

Particle acceleration by the Kelvin-Helmholtz instability at the magnetopause in the Double Mid-Latitude Reconnection configuration

M.H.J. Leroy,^{1, a)} B. Ripperda,¹ and R. Keppens¹

Centre for mathematical Plasma-Astrophysics, Department of Mathematics, KU Leuven, Celestijnenlaan 200B, B-3001 Leuven, Belgium

(Dated: 10 May 2022)

The importance of the role of the Kelvin-Helmholtz instability in the penetration of solar wind matter into the magnetosphere has been well demonstrated. In particular, the double mid-latitude reconnection (DMLR) process is a good candidate for an efficient exchange of matter through mixing and reconnection of the solar wind magnetic field into the magnetosphere. In this article, particle populations are introduced into different configurations and their trajectories are integrated using the guiding center approximation. The acceleration mechanisms taking place are studied and may help to identify specific signatures of the DMLR through particle characteristics. Their orbits appear to be influenced mainly by the magnetic curvature acceleration terms while their kinetic energy reduces. However, part of the particle population is driven into complex trapped trajectories, from which those particles escape with a gain in kinetic energy originating from the perpendicular gradient term.

Keywords: solar wind, magnetosphere, Kelvin-Helmholtz, particle acceleration

I. INTRODUCTION

Space weather around the Earth can cause threats for manned missions, spacecrafts as well as ground installations. One key mechanism is the solar wind (SW)/magnetosphere (MS) interaction as it determines the efficiency of the plasma transport process, an example being the Kelvin-Helmholtz instability (KHI) on the flanks of the magnetosphere^{1,2}. Through the double mid-latitude reconnection (DMLR) process³, the KHI can create configurations liable to magnetic reconnection and subsequent particle acceleration. The threats actually originate from those particles streaming through our magnetosphere with extremely high energy, while their trajectories and acceleration mechanisms are topics that are poorly understood thus far.

Many methods can be used to investigate charged particle trajectories in electromagnetic fields. The most descriptive methods can be found in fully kinetic particle-in-cell (PIC) codes (e.g. Noguchi et al.⁴, Guo et al.⁵ for relativistic plasmas and Markidis and Lapenta⁶, Li et al.⁷ for non-relativistic plasmas) in which both electrons and ions are treated as particles, and are iteratively moved while the electromagnetic fields are updated consistently. This is the most complete method, but the need to resolve the microscopic scales of the plasma leads to a very high computational cost. A hybrid approach is to treat the thermal part of the plasma as a fluid, like in the magnetohydrodynamics (MHD) framework, and the non-thermal particles with a PIC technique. The separation can either be based on the energy of the particles (e.g. Bai et al.⁸) or based on spatial separation of the regions where kinetic effects may play an important role (e.g. Daldorff et al.⁹, Makwana et al.¹⁰, Tóth et al.¹¹). There again

the constraint is related to the scales involved as a clear separation of MHD- and kinetic-scale physics has to be determined. In cases where the reconnection sites cannot be predicted and non-thermal particles could appear anywhere in the simulation domain, this would revert back to a full PIC simulation. In both types of models, the simulation domain is usually restricted to small scales, such that the large-scale processes as encountered in astrophysical phenomena cannot be captured.

These scales and computational cost constraints in combination with the fact that MHD simulations of the DMLR have already been thoroughly studied¹² led us to perform test particle simulations using the guiding center approximation (GCA) framework^{13,14}. The electrons and ions are embedded in a background thermal plasma, using results of previous fluid-based simulations¹², and the test particle trajectories are determined by the electromagnetic fields without feedback of the particles on the fields. In a plasma where the gradient of the magnetic field is larger than the gyration radius of the particle, the latter can be considered negligible and the GCA can be applied, allowing for the solution of a simplified set of equations and to determine adiabatic invariants for the particles. Details of the method and justifications of its use will be presented in Section II B.

The manuscript is organized as follows. In Section II we present the physical model and its numerical treatment along with the initial conditions devised to simulate the particles trajectories inside the DMLR. Section III exposes the resulting simulations as well as the statistical analysis of the particle ensemble. Section IV presents the different acceleration scenarios which can take place in the DMLR configurations.

^{a)}matthieu.leroy@kuleuven.be

II. PHYSICAL MODEL AND NUMERICAL SETTING

The simulations presented in this article were realized using the parallelized Adaptive Mesh Refinement Versatile Advection Code (MPI-AMRVAC)¹⁵ simulation toolkit¹⁶ for which the conservative Hall-MHD module (extension of MHD applicable to phenomena occurring on length scales shorter than the ion inertial length, and time scales shorter than the ion cyclotron period) has been tested and validated by Porth et al.¹⁷ and the particle module has been tested and applied by Ripperda et al.^{14,18,19}. This section will focus on the equations and initial settings directly related to our study.

A. Origin of the MHD background fields

The test particles are to be evolved in background electromagnetic fields which are extracted from our previous studies¹². In order to characterize how the instability can impact the trajectories of the particles, three different simulation times are selected representing three stages of the Kelvin-Helmholtz instability. A reference frame will be established by injecting $N_0=10000$ particles in a $t_{MHD}=0$ snapshot (where t_{MHD} is the normalized Alfvén time) of the simulation where the fields and thus the flanks of the magnetopause are unperturbed, and the influence of the instability will be investigated by injecting particles with the same initial conditions into snapshots at $t_{MHD}=400$ (rolling-up of the waves) and $t_{MHD}=600$ (non-linearly developed instability). Though the complete description and analysis of the selected fields can be found in the DMLR parameter study¹², the main features will be recalled here for clarity. The box size is chosen as $L_x=70$, $L_y=188$, $L_z=377$ (with $x \in [-40, 30]$, $y \in [-L_y/2, L_y/2]$, $z \in [-L_z/2, L_z/2]$), given in ion inertial lengths $\delta_i = c/\omega_p (\approx 100 \text{ km in near Earth conditions})$ and the number of cells in the simulations is $N^3=200^3$. The z -direction corresponds to the latitude and the y -direction follows the interface where the instability will develop, while the x -direction points across the shear layer. The simulation is initiated with analytical fields derived from the solution of a simplified Grad-Shafranov equation, that is invariant in the y -direction, and describes an initial equilibrium, such that the $\nabla \cdot \mathbf{B} = 0$ constraint is satisfied³. The magnetic fields and velocity are then derived from that vector potential $A_y(x, z) = (1/2)(4x/3 + L_x/(2\pi) \sinh((2\pi x)/L_z) \cos((2\pi z)/L_z))$ in the following fashion $B_x = -\partial A_y / \partial z$, $B_y = 0$, $B_z = -\partial A_y / \partial x$, $V_x = 0$, $V_y = (M_A/2) \tanh(A_y/L_u)$, $V_z = 0$. The velocity field is destabilized by incompressible perturbations $\delta A_y = \epsilon \sum_{m=1}^6 \left(\cos(2\pi mx/L_y) + \phi(m) \right) / m \times \exp(-(x/2L_u)^2) \times \exp(-(z/2L_u)^2)$ with amplitude $\epsilon=0.05$ and $\phi(m)$ a set of random phases. The density follows the same profile as the velocity, $\rho = (1/2)(\rho_c + 1) + (1/2)(\rho_c - 1) \tanh(A_y/L_u)$ ($\rho_c=4.7$

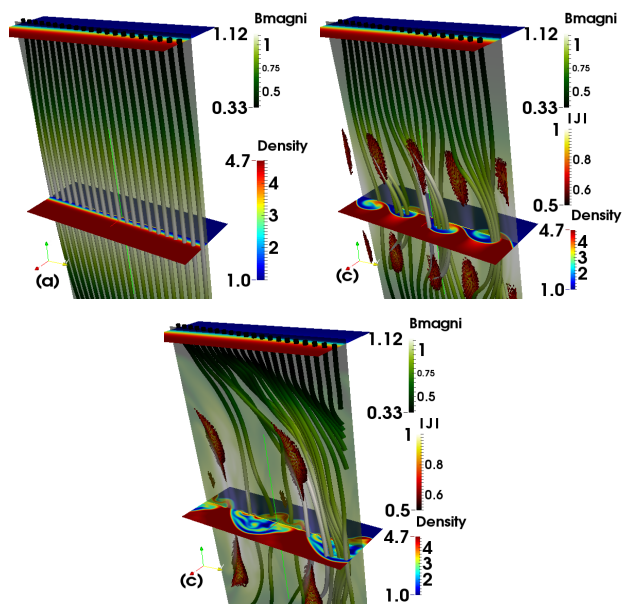


FIG. 1. Time evolution of the MHD simulation. Slices in the horizontal $x - y$ -plane present the density at different latitudes. Magnetic field lines are colored with magnetic field magnitude (in green), also represented by a slice in the vertical $y - z$ -plane. Points where the current magnitude is above 0.5 NU are displayed in shades of orange. Fig.(a) $t_{MHD}=0$, Initial configuration. Fig.(b) $t_{MHD}=400$, Rolling-up. Fig.(c) $t_{MHD}=600$, Mixing layer and strong current.

for the reference run, leading to an initial density contrast $\Delta_\rho=3.7$ with the SW presenting a higher density than the MS). The pressure is set as half the plasma parameter $\beta=0.71$ and is constant throughout the domain to respect the initial equilibrium. The other significant parameters set at the initialization of the simulations are the Alfvén Mach number $M_A=1$, the sonic Mach number $M_c=1$, the half-width of the shear layer $L_u=3$ and the polytropic index $\gamma_p=5/3$. The resistivity is chosen as $\eta=0.001$ to represent a nearly collisionless, weakly diffusive plasma. This initial condition induces a differential advection of the field lines as the flow evolves. Indeed the ‘high-latitude’ areas (edges of the box in the z -direction) are more stable with respect to the KHI than the domain closer to the $z=0$ plane, due to variations of the velocity and magnetic field magnitude. Thus vortices emerging near the $z=0$ plane locally advect the field lines while the part that is further away remains unperturbed for a longer time. The snapshots in Fig.1 show the selected background configurations from the MHD simulation in normalized units (NU). The horizontal slices are colored with the density (blue to red colorscale) and the current magnitude is displayed in surfaces in shades of orange. The magnetic field is represented by a slice in $y - z$ -plane and field lines in shades of green. The simulation box presents a symmetry with regards to the equatorial plane. At $t_{MHD}=0$ (Fig.1a) the initial configuration

displays nearly straight magnetic field lines, where the field is dominated by the z -component with its maximum value at $z=0$ and decreasing symmetrically towards the high latitudes. In the rolling-up stage ($t_{MHD}=400$, Fig.1b), the magnetic field lines relax around the crests of the waves, called spines of the KHI by Ma et al.²⁰, while they are compressed in the lower density (light blue) area of the waves. As a consequence of the creation of vortices, some field lines are starting to intersect at the latitudes where the flow turns from KHI unstable to KHI stable (latitude where the field lines turn from straight to bent). In the wake of the magnetic configuration change, current sheets start to form. In the last snapshot ($t_{MHD}=600$, Fig.1c), the rolled-up vortices have merged, inducing fewer but more extended current sheets with higher magnitude. The intersecting field lines obtain an even stronger curvature due to the differential advection. This process keeps increasing the tension between the field lines and reconnection sites are generated. Field lines that were previously connected to the magnetosphere are now linked to the solar wind, and vice versa, due to reconnection. This is called the DMLR phenomenon, studied by Faganello et al.³. It occurs around the current sheets for as long as the KHI vortices keep on braiding the field lines and the resulting effect is an almost regular and instantaneous exchange of matter and energy between the two regions. An extensive discussion of the fluid processes occurring, along with a detailed parameter study, can be found in our previous work¹².

B. Particle treatment and initial conditions

In order to integrate the trajectories of the test particles, the GCA¹³ will be used in this paper. This choice originates from the potential gain in computational cost this method can achieve but also from the fact that taking into account the scales and field magnitudes present in the MHD simulations, this approximation accurately describes the (charge q , mass m_0) particle trajectories. Indeed, if their gyroradius $r_g = \frac{m_0 v_{\perp}}{|q| B}$ and gyroperiod $\Omega = \frac{|q| B}{m_0}$ are much smaller than the length of the gradients and characteristic oscillation periods of the background electromagnetic fields, their motion can be decomposed into the trajectory of its guiding center and its gyration around this center, symbolized by a constant magnetic moment. It sums up to five equations describing the evolution of the guiding center position \mathbf{R} , the parallel momentum $p = m_0 \gamma v$ and the magnetic moment $\mu = m_0 \gamma^2 v_{\perp}^2 / (2B)$. The relativistic form²¹ will be used here for completeness and to investigate if there are any particles that can attain energies with a Lorentz factor $\gamma \gg 1$. The GCA equations can be written as:

$$\frac{\partial (m_0 \gamma^2 v_{\perp}^2 / (2B))}{\partial t} = 0, \quad (1)$$

$$\begin{aligned} \frac{\partial (m_0 \gamma v_{\parallel})}{\partial t} &= m_0 \gamma \mathbf{v}_E \cdot (\mathbf{v}_{\parallel} (\mathbf{b} \cdot \nabla) \mathbf{b} + (\mathbf{v}_E \cdot \nabla) \mathbf{b}) \quad (2) \\ &+ q E_{\parallel} - \frac{\mu}{\gamma} \mathbf{b} \cdot \nabla (\kappa B), \end{aligned}$$

$$\begin{aligned} \frac{\partial \mathbf{R}}{\partial t} &= \frac{(\gamma v_{\parallel})}{\gamma} \mathbf{b} + \frac{\mathbf{b}}{\kappa^2} \times \left\{ -\kappa^2 c \mathbf{E} \right. \\ &+ \frac{cm_0 \gamma}{q} \left(v_{\parallel}^2 (\mathbf{b} \cdot \nabla) \mathbf{b} + v_{\parallel} (\mathbf{v}_E \cdot \nabla) \mathbf{b} + v_{\parallel} (\mathbf{b} \cdot \nabla) \mathbf{v}_E \right. \\ &\left. \left. + (\mathbf{v}_E \cdot \nabla) \mathbf{v}_E \right) + \frac{\mu c}{\gamma q} \nabla (\kappa B) + \frac{v_{\parallel} E_{\parallel}}{c} \mathbf{v}_E \right\}, \end{aligned} \quad (3)$$

where q is the electrical charge, m_0 is the rest mass, v_{\parallel} and v_{\perp} are the velocities parallel and perpendicular to the magnetic field respectively, $\mathbf{b} = \mathbf{B}/B$ is the unit vector in the direction of the magnetic field, c is the speed of light and $\gamma = 1/\sqrt{1 - v^2/c^2}$ is the Lorentz factor. The term $\mathbf{v}_E = \mathbf{E} \times \mathbf{B}/B^2$ is the drift velocity induced by the $\mathbf{E} \times \mathbf{B}$ field and κ its Lorentz factor.

The governing equations are solved using a fourth-order Runge-Kutta scheme with adaptive time-stepping and the field values are interpolated to first order after being scaled to CGS units, from the normalized MHD simulations. The typical timestep for the evolution of the variables related to particles is much smaller than the MHD timestep so the MHD fields can be considered static. We evolve electrons, because their gyroradius is smaller and thus the guiding center approximation holds better than for heavier ions. Moreover, since electrons are faster, they will have a longer trajectory in the same physical time, allowing them to cover more of the physical domain and thus giving us access to the various processes that can be encountered. Since we are interested in the effects of the reconnection events happening at mid-latitude in the MHD snapshots, particles are initiated within a narrow band of the following dimensions $x \in [2, 8]$, $y \in [-L_y/2, L_y/2]$, $z \in [25, 85]$, defined to encompass the more intense part of the current sheets present at $t_{MHD}=400$ and $t_{MHD}=600$. Their velocities are initiated following a Maxwellian distribution and with random directions. With typical values of the SW/MS interface²² $v_{\perp} \sim 40 \text{ km/s}$ and $B=40 \text{ nT}$, the gyroradius for electrons is of the order $r_g \sim 10 \text{ m}$, while the cell size are of the order of $\delta_i = 10^5 \text{ m}$. So even if the particles are accelerated to non-thermal velocities, the gyroradius may increase up to several orders until the GCA fails.

III. STATISTICAL ANALYSIS

A first approach to evaluate the effect of the three configurations is to analyze statistically the evolution of the particle population. Fig.2 displays the initial particle population spectrum of (mass-scaled scaled) kinetic energy ($E_k = v_{\parallel}^2 + v_{\perp}^2$) along with the $t_p=1$ and $t_p=2$ spectra for the three MHD snapshots. The initial Maxwellian

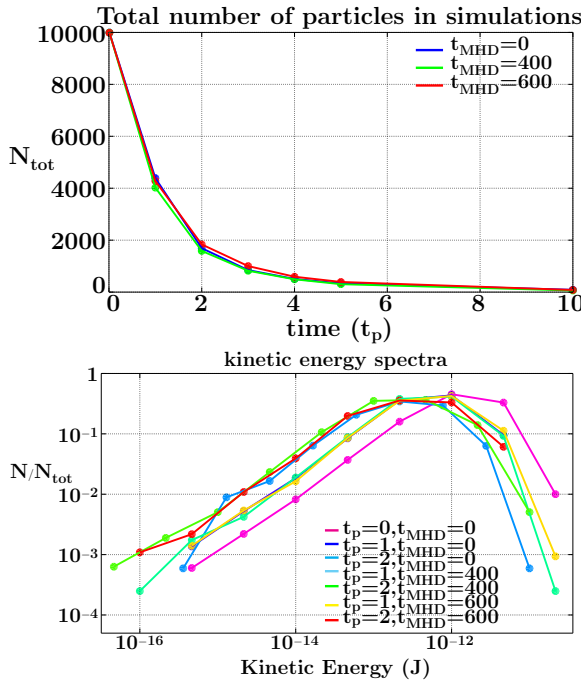


FIG. 2. (top) Number of remaining particles in the simulation domain as times advances. (bottom) Kinetic energy spectra of the particle population at different times in the particle simulation for the three MHD snapshots.

characteristic is conserved as the particles evolve, although in all cases the distributions shift towards smaller energies, indicating a global loss of kinetic energy for the particle population. While the simulation aims to advance the particles to $t_p=20$, the spectra displayed are limited to $t_p=2$. This is because after that point there is not enough particles left in the simulation domains to establish correct statistics, as shown in Fig.2 (top). There are two causes for the particles to disappear from the simulation box. The first is that they escape through the back and front of the domain as our boundary conditions in the x -direction are open. Our initial conditions result in an hourglass shape for the magnetic field lines, with the narrowest part located on the equatorial plane. Therefore, several field lines connect a $z > 0$ part of the front (or back) edge to $z < 0$ part. Particles that are initially on these fields lines rapidly exit the simulation. The second cause is related to the code implementation. Particles are evolved separately in parallel and their time step is adaptive. For some particles, this timestep becomes very small and their integration cannot be completed before the end of the allowed computing time. In that case, they are still in the simulation box, but they do not appear anymore in the files for larger t_p .

Another method to understand how the particle population is driven by the MHD configurations is to establish the spectra of the acceleration terms (conform to the terms in Eq.(2)) and to determine which dominate. These mechanism are the parallel magnetic gradient or

mirroring term ($\mathbf{b} \cdot \nabla(\kappa B)$, dubbed *gradb* in Fig.3), the resistive field acceleration term (qE_{\parallel} , *resist*) and the curvature terms ($\mathbf{v}_E \cdot [(\mathbf{v}_E \cdot \nabla)\mathbf{b}]$, *b.curvb* and $\mathbf{v}_E \cdot [(\mathbf{b} \cdot \nabla)\mathbf{b}]$, *ue.curvb*). Fig.3 presents the spectra of the momentum magnitude for the terms of Eq.(2) for the three configurations at $t_p=2$, since at this point the particle population had time to evolve and diverge from its initial spatial distribution and energy spectrum. In the $t_{\text{MHD}}=0$ spectrum, the electric field acceleration and parallel gradient terms are slightly dominant while the curvature terms have their peaks at a lower energy while still present in the highest energy area. It is coherent with Fig.1 where the MHD background acts as magnetic trap with the field line's density and magnitude increasing toward the equatorial plane. It appears that the particle population is bouncing around a magnetic trap and is accelerated in the middle by an electric field, while slowly drifting. The curvature terms are present because of the hourglass shape of the magnetic field discussed earlier, and spread because many particles are on these bent field lines that lead them out of the box. In the two other cases, the curvature terms are largely dominant, which is again coherent with Fig.1 displaying twisted field lines. In these configurations, the particles are bouncing in the mirror trap while following strongly curved trajectories with drifts caused by the large magnetic gradients. The situation is actually the same for the three configurations with particles mirroring between two extrema and getting accelerated by an electric field. However, in the more complex configurations, the trajectories are more intricate as well and are largely influenced by the gradient terms.

An oversight of any statistical study is that spectra only give information about the state of the whole population at a given instant. Since the particles are mostly following periodic orbits, the forces they actually experience display periodicity and local variations in magnitude as well. This calls for a particle-by-particle analysis in order to clearly assess which processes determine their individual acceleration or deceleration scenarios.

IV. INDIVIDUAL PARTICLES TRAJECTORIES AND ACCELERATION MECHANISMS

Particles evolving in our electromagnetic background fields are seldom subject to one or another acceleration mechanism in a simple manner. The analysis of individual particle trajectories should inform us on the precise ways and times the different momentum contributions act on them and which mechanisms could accelerate particles. It is reminded here that particles that cross the top or bottom edges of the domain can evidently not come back from the other side in reality. The periodic boundary conditions in the y - and z -direction allow for them to remain in the simulation box, consistently with the periodic boundaries applied in the MHD study, as the focus of the study is on processes taking place around the

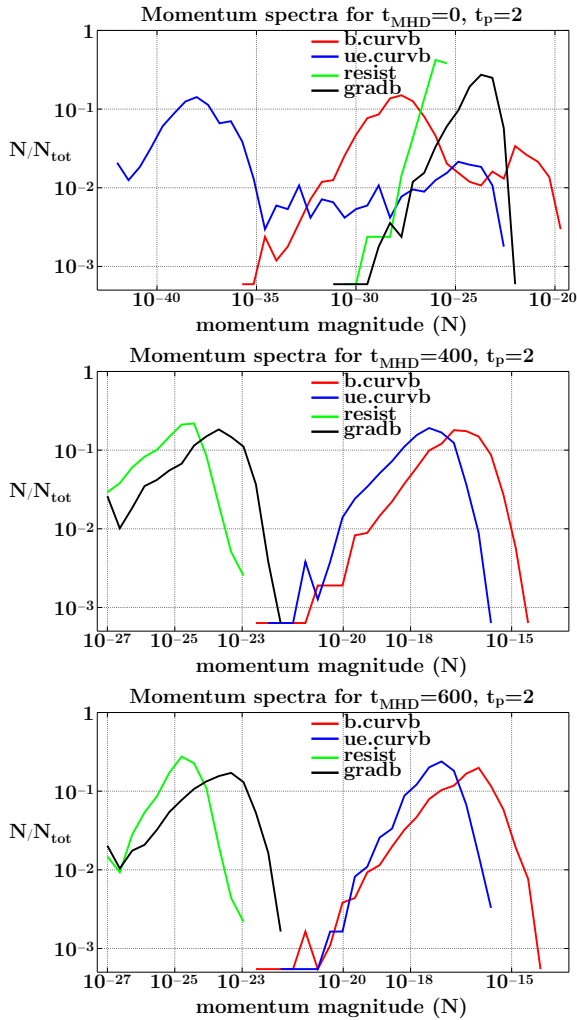


FIG. 3. Momentum spectra at $t_p=2$ for the 3 MHD configurations. Parallel magnetic gradient ('gradb'), resistive field acceleration term ('resist'), the curvature terms ('b.curvb', 'ue.curvb'). The curvature terms dominate the particles dynamics with field lines bending more and more.

equatorial and mid-latitude region. Those can be considered as beams of particles launched into the simulation with the same direction but different initial positions.

Fig.4 displays the trajectories colored with time of 2 particles, chosen because they represent the trajectories that typically develop in our study. Each particle displayed has the same initial position and velocity across the simulations with the three different backgrounds. As has been hinted by the analysis of the spectra, the trajectories are different between the $t_{MHD}=0$ simulations and the others. Fig.4.(a) shows the only two possible types of trajectories for the $t_{MHD}=0$ state. The first kind of particles are trapped in mirroring trajectories away from the equatorial plane like p1, where complete mirroring occurs at a finite distance from the equatorial plane. Those particles bounce back and forth in the magnetic bottle created by the larger magnitude of the magnetic field around

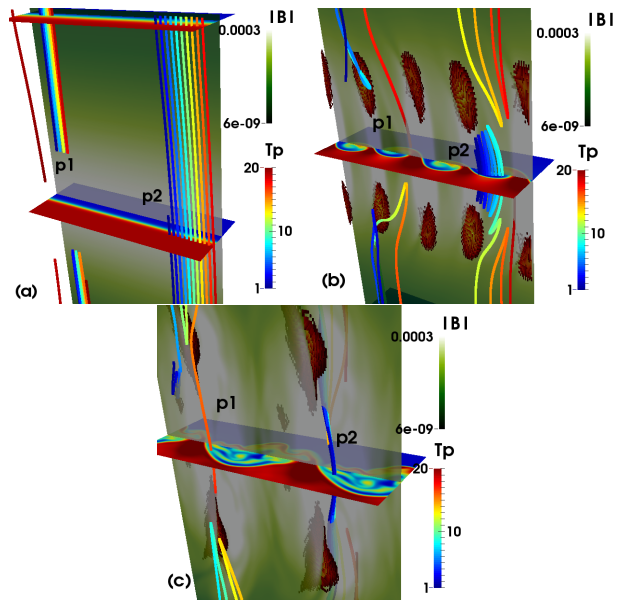


FIG. 4. Trajectories for particles p1 and p2, colored with time for the 3 configurations. All other colors have the same meaning as Fig.1

$z=0$, and their individual excursion in the z -direction is determined by their initial energy. The second kind are streaming across the domain like p2 when their energy is sufficient to escape the magnetic trap. Note also the small drift in the direction perpendicular to the (mainly vertical) magnetic field as time progresses, due to the $\mathbf{E} \times \mathbf{B}$ contribution. This is coherent with the initial topology constituted by a large z -component of the magnetic field with areas of larger values of the x -component around the mid-latitudes, creating the mirror trap. This also explains the predominance of the mirroring and electric acceleration term in the spectrum of Fig.3.

Fig.4.(b) illustrates how the mirroring particle trajectories are modified by the bending of the magnetic field lines. The curvature terms are also more dominant (see Fig.3.(b)) and those particles can drift much further to other field lines. It also introduces particles temporarily trapped between the current sheet latitudes (p2). As can be seen from the trajectories of both particles, it is easier to penetrate the equatorial region when passing between the current sheet regions, which corresponds to regions of lower magnitude of the magnetic field. Particles coming from the exterior can get trapped in the equatorial region, or escape if they drift until they find an easier path through the magnetic trap (p2).

Fig.4.(c) completes Fig.4.(b) by showing that particles can get trapped in smaller regions close to the current sheet, like for p1 at the beginning of the simulation. It demonstrates how the locations where a particle bounces back or passes through the magnetic trap can be very close. It also shows that the overall statistics can hide specifics of the trajectories, as this time p1 is trapped and escapes while p2 passes through or mirrors outside the

mid-latitude. The statistics for the two configurations are almost similar, despite individual particles presenting totally different trajectories when interacting with the different backgrounds.

To sum up, when the magnetosphere is in a quiet configuration, particles evolve in a large magnetic trap. If the Kelvin-Helmholtz instability develops and starts twisting the field lines at the interface, the conditions for more complex trajectories emerge and new acceleration mechanisms becomes important. The particles encounter higher magnetic gradients and electric fields (current sheets) in larger and more frequent spots, leading to the increase of the drift magnitude and the complexity of the magnetic trap that can cause particles to get trapped near the equatorial region.

A. Accelerated particles

In this section, the different types of trajectories will be examined to identify the mechanisms affecting the particle's gain or loss of kinetic energy. The time evolution of their position, kinetic energy and the electromagnetic fields they encounter will be compared against the different terms directly affecting the kinetic energy variations. Indeed, combining Equations (1) and (2), an expression for the energy change rate can be derived (from Zhou et al.²³ with additions) :

$$\frac{\partial E_k}{\partial t} = \frac{m_0}{2} \frac{\partial(\gamma v_{\parallel})^2}{\partial t} + \frac{m_0}{2} \frac{\partial(\gamma v_{\perp})^2}{\partial t}, \quad (4)$$

$$\frac{m_0}{2} \frac{\partial(\gamma v_{\perp})^2}{\partial t} = \mu v_{\parallel} (\mathbf{b} \cdot \nabla) B + \mu (\mathbf{v}_E \cdot \nabla) B, \quad (5)$$

$$\begin{aligned} \frac{m_0}{2} \frac{\partial(\gamma v_{\parallel})^2}{\partial t} &= q\gamma v_{\parallel} E_{\parallel} + m_0(\gamma v_{\parallel})^2 \mathbf{v}_E \cdot [(\mathbf{b} \cdot \nabla) B] \\ &+ m_0\gamma^2 v_{\parallel} \mathbf{v}_E \cdot [(\mathbf{v}_E \cdot \nabla) B] - \mu v_{\parallel} \mathbf{b} \cdot \nabla(\kappa B). \end{aligned} \quad (6)$$

It is verified that for any particle in all runs, $\gamma \sim 1$ and hence $\kappa \sim 1$. Eq.(5) and Eq.(6) can thus be substituted into Eq.(4) to obtain a final expression for the kinetic energy evolution:

$$\begin{aligned} \frac{\partial E_k}{\partial t} &= qv_{\parallel} E_{\parallel} + \mu(\mathbf{v}_E \cdot \nabla) B + m_0 v_{\parallel}^2 \mathbf{v}_E \cdot [(\mathbf{b} \cdot \nabla) B] \\ &+ m_0 v_{\parallel} \mathbf{v}_E \cdot [(\mathbf{v}_E \cdot \nabla) B]. \end{aligned} \quad (7)$$

This equation confirms that even if the parallel magnetic gradient $\mathbf{b} \cdot \nabla B$ can act on v_{\parallel}^2 and v_{\perp}^2 variations, it has no effect on the total kinetic energy. The remaining terms express the resistive electric field, the perpendicular magnetic gradient and the curvature terms contributions respectively (identified as *resist*, *gradb*, *b.curvb* and *ue.curvb* in the figures).

Fig.5 presents those quantities for p1 and p2 from Fig.4(a), focused on one travel between two edges. In this figure as well as the following ones, black vertical lines indicate specific times (coinciding with local extrema) in the evolution and facilitate the comparison between

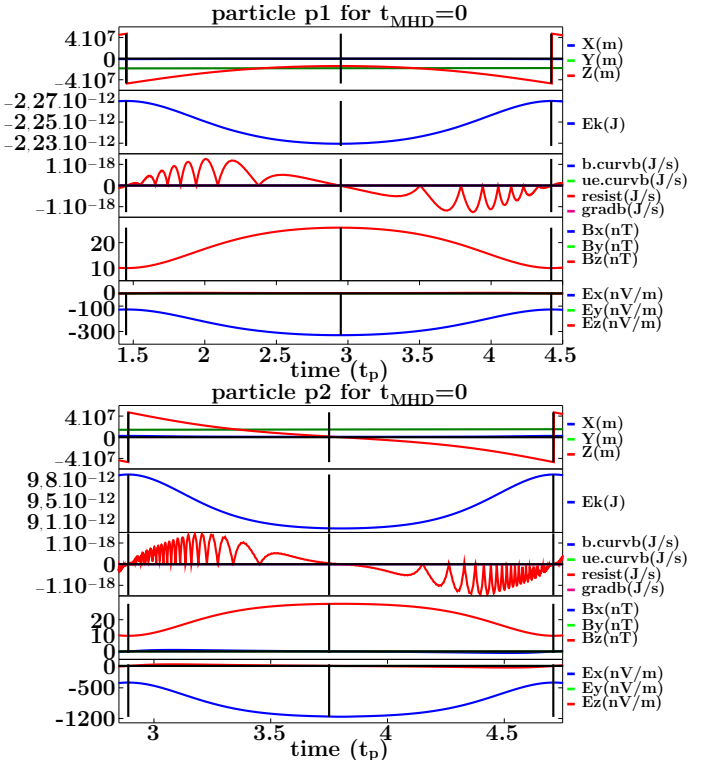


FIG. 5. Positions, kinetic energy, ΔE_k contributions and electromagnetic fields encountered components for particles p1 (top) and p2 (bottom) at $t_{MHD}=0$.

quantities. In the same spirit, a black horizontal line in each graph indicates the zero value for all quantities. It can easily be observed that the curves present similar evolutions with the kinetic energy reaching an extremum at the time the magnitude of the electromagnetic fields are maximum. The main difference is the larger value of kinetic energy for p2 than for p1, allowing the particle to pass through the equatorial plane instead of undergoing the mirror turn-around like p1. The x -component of the electric field seen by p2 is also 4 times larger, which is in accord with the larger $\mathbf{E} \times \mathbf{B}$ drift visible for its trajectory.

In the $t_{MHD}=400$ configuration, particles are exhibiting different mirroring and passing trajectories, as shown for 2 new particles p3 and p4 in Fig.6. Particle p4 exhibits a bouncing trajectory but passes through the magnetic trap when its angle of approach is slightly different. It presents how the curvature terms are driving particles to follow the field lines in their twisted configuration. The rebound takes place when going towards regions of large magnetic field, surrounded by the current sheets, while the particle can cross the equatorial plane when it is oriented towards a weaker magnetic field by bending around the current sheets. Particle p3 re-visits this point in a different fashion as particles, coming from positions fairly spread out, are funneled through a particularly narrow area between current sheets. The detailed analysis of parts of these trajectories reveals another difference

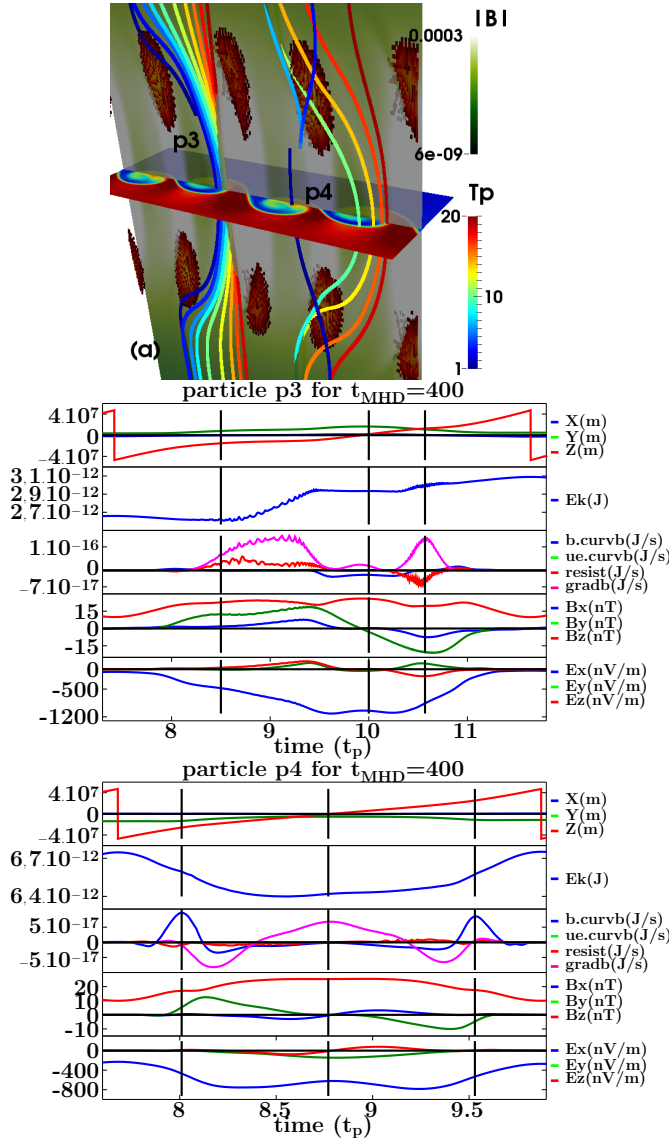


FIG. 6. Trajectories (top, colored with time), positions, kinetic energy, ΔE_k contributions and electromagnetic fields encountered components for particles p3 (middle) and p4 (bottom) at $t_{MHD}=400$.

between them. While both are crossing the equatorial plane from bottom to top and evolve through very similar electromagnetic fields, their kinetic energy evolution is different. The curves for p4 display on either side of $z=0$ symmetrical fields and contributions, dominated by the $gradb$ and $b.curvb$ terms. Although its energy is decreased while going from $z=-L_z$ to $z=0$, it is restored when going from $z=0$ to $z=+L_z$. It is interesting to see that the same profile of the magnetic gradient and curvature terms from Eq.(7) can either decrease or increase the energy of the particle, depending on the direction in which the particle is traveling through the fields. For example, the energy for p3 increases by 15% in two steps coinciding with peaks of the $gradb$ and $resist$ terms and

larger value of the electric field while the particle is at the latitude of the current sheets. The increase is larger when both dominating contributions are both positive, indicating that the *resist* term can influence the energy both ways for the passing trajectories, while the *gradb* term keeps the same sign as the y -component of the electric field. While both particles go through the domain on their typically bent trajectories, the resulting variations of kinetic energy and the related contributions can be very different depending on the combination of electromagnetic components they encounter.

The next particles relate to a class of trajectory that is specific for the perturbed MHD configurations. Particles p2, p5 and p6 are trapped inside the equatorial region, either starting there and escaping (p2, p5), or coming from outside and getting trapped (p6), as can be seen in Fig.7. Despite sharing this characteristic, these particles still exhibit different behaviors while being trapped. Particle p5 crosses the equatorial plane inside a Kelvin-Helmholtz vortex, its trajectory bends to the left and it continuously gains kinetic energy (up to 15%) before escaping next to a current sheet. This kinetic energy increase is driven by the positive value of the $gradb$ term. Particle 2 is trapped around a low density area, bends to the right and loses energy before it gains energy again (13%) when the $gradb$ term from Eq.(7) becomes positive and finally, it escapes between two current sheets. Lastly, particle p6 gets trapped when bouncing near a current sheet to adopt a trajectory similar to p2 and loses kinetic energy as well before re-gaining energy, at late times in the simulation. In all cases, the variations of the $gradb$ contribution drives the variations of kinetic energy, which increases when this term is positive, and decreases when $gradb$ is negative. Those variations also appear to be related to the variations of sign of the y -component of the electric field. While the other components, magnetic or electric, are apparently oscillating with no coherence with the $gradb$ contribution, this component shows a clear link with its variation, despite the complexity of this term.

Lastly, Fig.8 displays two particles trapped around the equatorial plane for $t_{MHD}=600$. While sharing a very similar trajectory in the same region of the MHD background, their kinetic energy variations follow the opposite values of the $gradb$ contribution due to the exact topology of the fields they cross. Particle p8 demonstrates large energy gain when crossing the $z=0$ plane, due to the large peaks in the $gradb$ term, occurring when several components of the magnetic and electric fields change sign. Particle p7 sees similar profiles and sign changes but the fact that they do not happen at the exact same time (like p8) results in different peaks of the $gradb$ term and hence it loses energy each time it crosses the equatorial plane.

While the kinetic energy variations seem to be closely related to one specific contribution, there are various ways this term influences the trajectories and even similar trajectories can exhibit either energy gains or losses. All these mechanisms are still for the most part only frac-

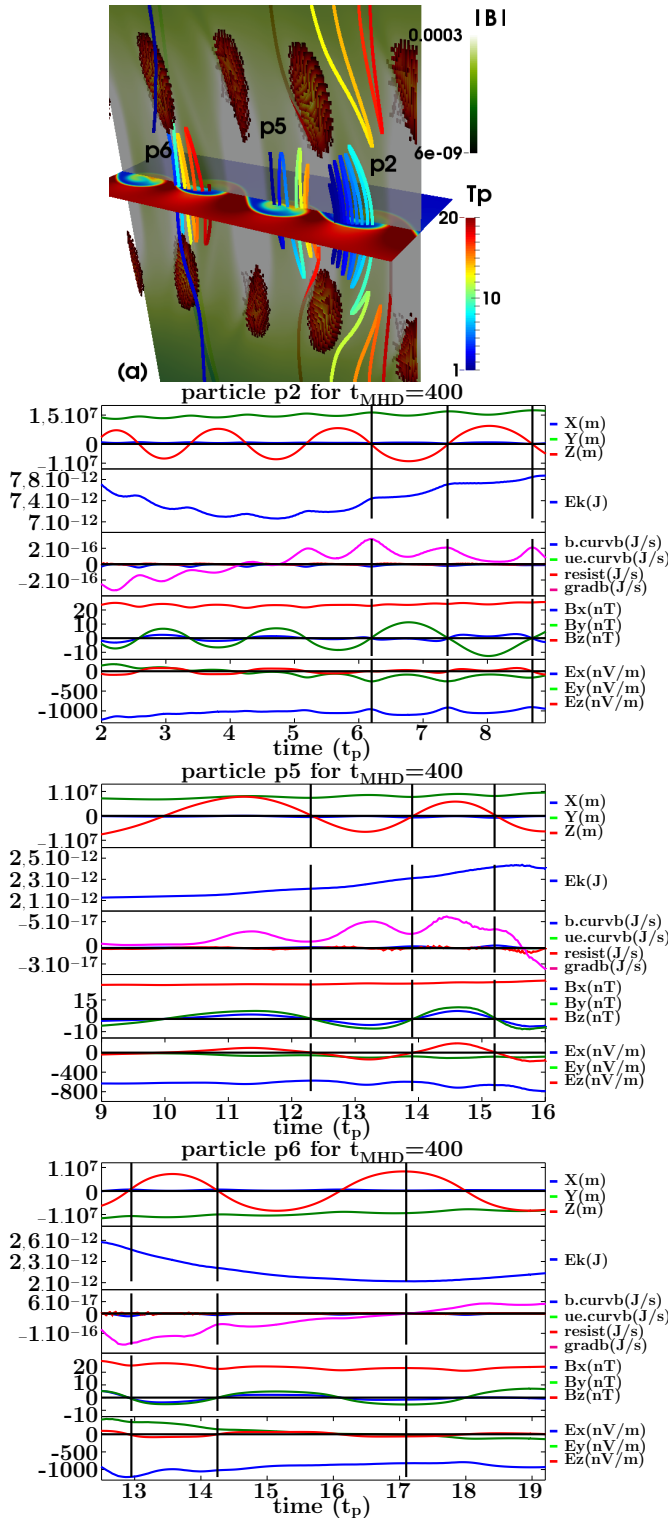


FIG. 7. Trajectories (top, colored with time), positions, kinetic energy, ΔE_k contributions and electromagnetic fields encountered components for particles p2 (second figure), p5 (third figure) and p6 (bottom) at $t_{MHD}=400$.

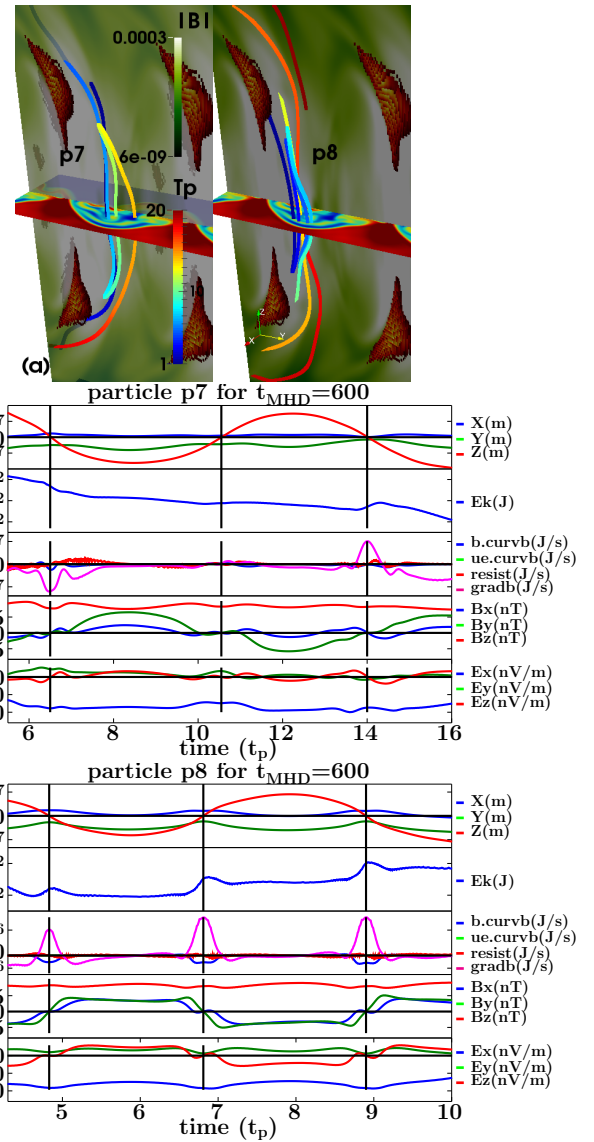


FIG. 8. Trajectories (top, colored with time), positions, kinetic energy, ΔE_k contributions and electromagnetic fields encountered components for particles p7 (middle) and p8 (bottom) at $t_{MHD}=600$.

tions of a full particle trajectory since actual particles will not remain trapped forever in the equatorial plane. This specific issue is addressed in the next section.

B. The 'catch and release' process

Up to now, particle trajectories showed only one feature each, either mirroring, passing or in a magnetic trap. A few particles completed trajectories that includes a full travel through the domain with a trapped episode. Those can give more insight in the process of passing through the equatorial trap and how it affects their kinetic energy.

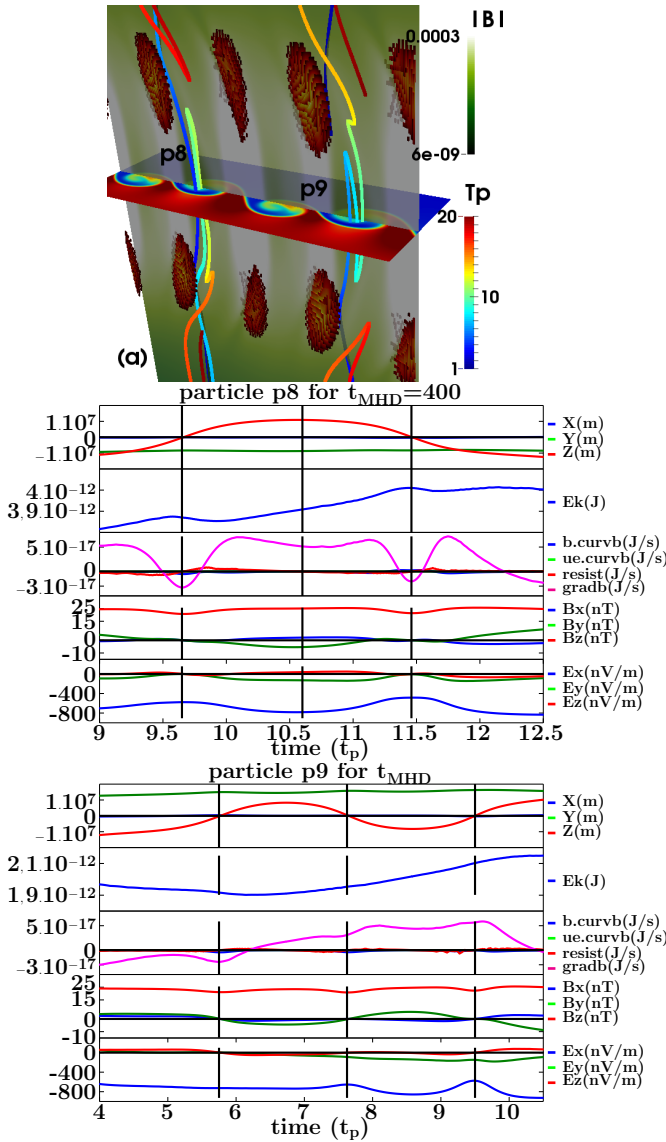


FIG. 9. Trajectories (top, colored with time), positions, kinetic energy, ΔE_k contributions and electromagnetic fields encountered components for particles p8 (middle) and p9 (bottom) at $t_{MHD}=400$.

Fig.9 displays two particles for $t_{MHD}=400$ that are first getting trapped in the equatorial region, from which they escape afterwards. Both have a similar trajectory, entering from the bottom of the region after bending around a current sheet, except for the fact that p9 escapes from the top while p8 continues its trajectory returning to the bottom of the domain. Both particles are remaining between the mid-latitudes for a short period, but both exhibit a net gain in kinetic energy. This is again correlated with a positive value of the $gradb$ term and negative value of the y -component of the electric field. The same way, p2, p5 and p6 in Fig.7 all showed an energy gain if they remain long enough in the equatorial magnetic trap, even if they lost some of it when entering it. It would seem that par-

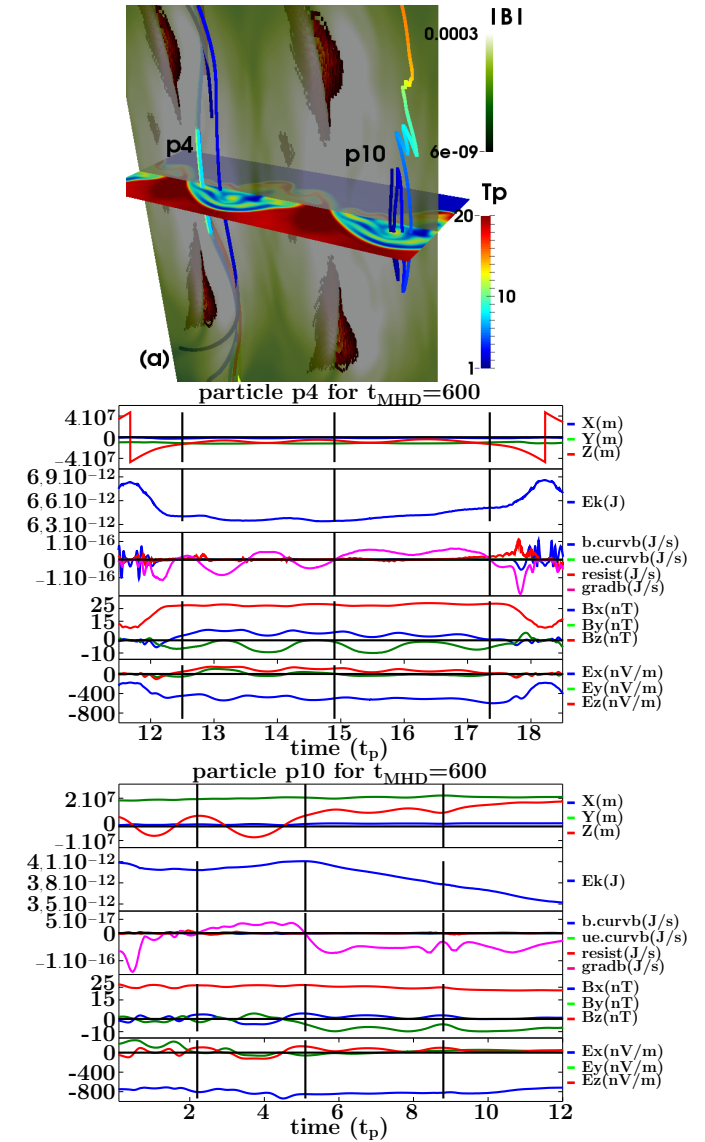


FIG. 10. Trajectories (top, colored with time), positions, kinetic energy, ΔE_k contributions and electromagnetic fields encountered components for particles p4 (middle) and p10 (bottom) at $t_{MHD}=600$.

ticles will mostly get accelerated after being caught and released from the equatorial region. This result is confirmed by the particles in Fig.10, where they both exhibit an energy gain while trapped around the equatorial plane. However, both particles lost energy when they are caught, and lose a much larger quantity in the subsequent secondary traps near the current sheets. The variations of the kinetic energy are still closely related to the sign of $gradb$ and the y -component of the electric field. Part of the explanation for these different trajectories lies in the perturbations to the configuration of the magnetic field driven by the KHI. Fig.11 presents an isosurface of the magnetic field, colored by its x -component. The current sheets and passing tra-

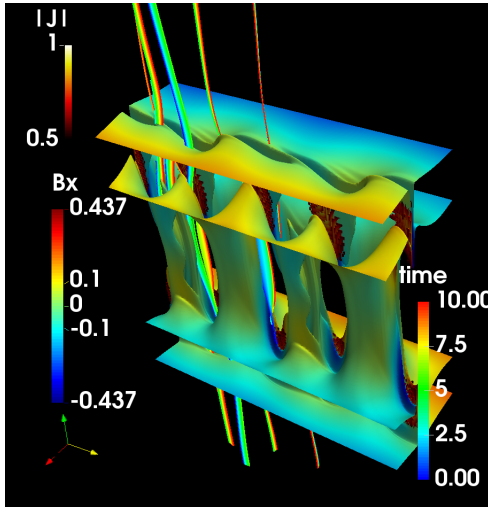


FIG. 11. Magnetic field topology, $t_{MHD}=400$.

jectory particles are included as well, to illustrate how particles get trapped or not. By compressing more or less the field lines, the KHI vortices create areas of lower magnetic field, connected to narrower areas around the current sheets. Those paths are ways for the particles to pass through the trap, but due to drifting effectd, some do not follow symmetric trajectories. Those particles get caught and they drift until they can escape the trap, most of the time gaining energy in the process.

V. CONCLUSIONS

In this paper, charged particle trajectories in the DMLR, as caused by the Kelvin-Helmholtz instability at the MS/SW interface were presented. A statistical and individual analysis was conducted in order to identify specific acceleration mechanisms. It was found that the perpendicular magnetic gradient term from Eq.(7) was mainly responsible for the variations of the kinetic energy, with a link to the sign of the y -component of the electric field, though the results can show exceptions to this process. Particles that are getting caught in the area between the current sheets latitude mostly gain energy during a bouncing trajectory before their release into the outer domain. It appears that the cavities created by the Kelvin-Helmholtz vortices in the equatorial plane can be regions where electrons can gain energy. This study should be confirmed by simulations including a more realistic resistivity, a dynamic rather than a static MHD evolution, and a larger MHD resolution to see the additional effects of the reconnection in the current sheet on the particle acceleration.

ACKNOWLEDGMENTS

This research was supported by GOA/2015-014 (2014-2018 KU Leuven). The simulation were performed on KU Leuven Tier-1 High Performance Computing cluster BrE-niac, as the computational resources and services were provided by the VSC (Flemish Supercomputer Center), funded by the Research Foundation Flanders (FWO) and the Flemish Government - department EWI. The figures in this paper were realized using the GNU software Octave²⁴, the Matlab software and the open-source visualization software Paraview²⁵.

- ¹J. W. Dungey, in *Physics of the Magnetosphere* (Springer, 1968) pp. 218–259.
- ²H. Hasegawa, M. Fujimoto, T.-D. Phan, H. Reme, A. Balogh, M. Dunlop, C. Hashimoto, and R. TanDokoro, *Nature* **430**, 755 (2004).
- ³M. Faganello, F. Califano, F. Pegoraro, and T. Andreussi, *EPL (Europhysics Letters)* **100**, 69001 (2012).
- ⁴K. Noguchi, C. Tronci, G. Zuccaro, and G. Lapenta, *Physics of plasmas* **14**, 042308 (2007).
- ⁵F. Guo, Y.-H. Liu, W. Daughton, and H. Li, *The Astrophysical Journal* **806**, 167 (2015).
- ⁶S. Markidis and G. Lapenta, *Journal of Computational Physics* **230**, 7037 (2011).
- ⁷X. Li, F. Guo, H. Li, and G. Li, *The Astrophysical Journal Letters* **811**, L24 (2015).
- ⁸X.-N. Bai, D. Caprioli, L. Sironi, and A. Spitkovsky, *The Astrophysical Journal* **809**, 55 (2015).
- ⁹L. K. Daldorff, G. Tóth, T. I. Gombosi, G. Lapenta, J. Amaya, S. Markidis, and J. U. Brackbill, *Journal of Computational Physics* **268**, 236 (2014).
- ¹⁰K. Makwana, R. Keppens, and G. Lapenta, *Computer Physics Communications* **221**, 81 (2017).
- ¹¹G. Tóth, X. Jia, S. Markidis, I. B. Peng, Y. Chen, L. K. Daldorff, V. M. Tenishev, D. Borovikov, J. D. Haiducek, T. I. Gombosi, *et al.*, *Journal of Geophysical Research: Space Physics* **121**, 1273 (2016).
- ¹²M. H. J. Leroy and R. Keppens, *Physics of Plasmas* **24**, 012906 (2017), <http://dx.doi.org/10.1063/1.4974758>.
- ¹³T. G. Northrop, *The Adiabatic Motion of Charged Particles*, 21 (Interscience Publishers, 1963).
- ¹⁴B. Ripperda, F. Bacchini, J. Teunissen, C. Xia, O. Porth, L. Sironi, G. Lapenta, and R. Keppens, *The Astrophysical Journal Supplement Series* **235**, 21 (2018).
- ¹⁵R. Keppens, Z. Meliani, A. J. van Marle, P. Delmont, A. Vlasis, and B. van der Holst, *Journal of Computational Physics* **231**, 718 (2012).
- ¹⁶Toolkit and manual available in open source at <http://gitlab.com/mpi-amrvac/amrvac>.
- ¹⁷O. Porth, C. Xia, T. Hendrix, S. Moschou, and R. Keppens, *The Astrophysical Journal Supplement Series* **214**, 4 (2014).
- ¹⁸B. Ripperda, O. Porth, C. Xia, and R. Keppens, *Monthly Notices of the Royal Astronomical Society* **467**, 3279 (2017).
- ¹⁹B. Ripperda, O. Porth, C. Xia, and R. Keppens, *Monthly Notices of the Royal Astronomical Society* **471**, 3465 (2017).
- ²⁰X. Ma, A. Otto, and P. A. Delamere, *Journal of Geophysical Research: Space Physics* **119**, 781 (2014).
- ²¹P. O. Vandervoort, *Annals of Physics* **10**, 401 (1960).
- ²²M. Øieroset, T. Phan, V. Angelopoulos, J. Eastwood, J. McFadden, D. Larson, C. Carlson, K.-H. Glassmeier, M. Fujimoto, and J. Raeder, *Geophysical Research Letters* **35** (2008).
- ²³X. Zhou, J. Büchner, M. Bárta, W. Gan, and S. Liu, *The Astrophysical Journal* **827**, 94 (2016).
- ²⁴S. H. John W. Eaton, David Bateman and R. Wehbring, *GNU Octave version 3.8.1 manual: a high-level interactive language*

for numerical computations (CreateSpace Independent Publishing Platform, 2014) ISBN 1441413006.

²⁵J. Ahrens, B. Geveci, C. Law, C. Hansen, and C. Johnson, “36-paraview: An end-user tool for large-data visualization,” (2005).

²⁶T. Akramov and H. Baty, Physics of Plasmas **24**, 082116 (2017), <https://doi.org/10.1063/1.5000273>.